

THREE-DIMENSIONAL SAR WITH FIXED TRANSMITTER AND ITS SCATTERING EXPLANATION

J. Shi^{*}, K. Liao, and X. Zhang

School of Electronic Engineering, University of Electronic Science and Technology of China, Chengdu 611731, China

Abstract—During the experimental data processing, we find that corner reflectors cannot be focused properly using 3-D SAR with a moving transmitter due to the phase reversal phenomenon based on the phase history analysis, i.e., the phases at different observation angles might shift rad, and the echoes cancel, rather than accumulate, to each other. To overcome this defect, 3-D SAR with fixed transmitter is designed. Since the geometry of the transmitter and targets remains unchanged during the observation session, the coherence of echoes is well preserved. The mechanism of 3-D SAR with fixed transmitter can accurately be explained using the Stratton-Chu equation. For perfect conductor, the 3-D image is related to the electric current density. For general dielectric medium, the 3-D image is related to the electric current density, magnetic current density and directional vector of scatterer. Experimental results show that one can focus corner reflectors and cavity-shaped objects by fixing the transmitter, which might fail for the traditional 3-D SAR because of the phase reversal phenomenon.

1. INTRODUCTION

With the ability of three-dimensional (3-D) resolution, 3-D microwave imaging technique becomes one of the hot points in the radar and electromagnetic societies. In recent years, some experiments with different working modes [1–12] have been carried out, fine-resolution and high-quality images have been presented in literatures [5]. In the field of remote sensing, 3-D SARs, such as linear array SAR [3], can overcome the shading-effect via down-looking mode, which are more feasible for observing the mountain and urban areas and

Received 14 August 2012, Accepted 7 October 2012, Scheduled 22 October 2012

* Corresponding author: Jun Shi (cn.papyrus@yahoo.com.cn).

extracting the DEM of steep terrain. In the field of electromagnetic (EM) measurement, They can also be used for radar absorbing material/antenna RCS measurement and inspection, stealth structure analysis, security inspection, etc. [5].

The basic idea of microwave 3-D imaging technique is to acquire the scattering electric field in a large 2-D/3-D spatial scale, and reconstruct the target's shape and scattering characteristics by signal processing techniques, typically based on the principle of matched filtering [13]. The data acquisition can be fulfilled by a large-size real antenna array or synthetic aperture technique [12], which moves the antenna(s) in 2-D/3-D space to compose a virtual antenna array. Compared with real antenna arrays, synthetic aperture technique is relatively simpler and cheaper, which is more feasible in practice.

According to the imaging results [5], however, though the system's resolution is extremely high, the images of the fighting vehicle in some aspects cannot reflect its real shape. The one reason is that the target's EM characteristic is different from its optical characteristic. On the other hand, the spatial variation of scattering characteristic should also be considered during 3-D SAR system design. When the synthetic aperture angle is small, the variation can be ignored. In high-resolution condition, however, the synthetic aperture angle is rather large, and the variation will cause the acquired data non-coherent, and deteriorate the image quality greatly.

To eliminate the variation of scattering characteristic, an easy-to-understand method is to fix the transmitter, rather than move synchronously with the receiver. Since the transmitted signal and the geometry of the transmitter and targets remain unchanged during the observation session, the coherence of scattering electric field is well preserved, which is crucial for SAR system. Under this consideration, the mechanism of 3-D SAR imaging can be explained using the scattering theory, which separates the scattering phenomenon into two stages:

Firstly, the incident electromagnetic wave inspires the induced electric/ magnetic currents on the targets,

Secondly, the induced electric/magnetic currents produce the scattering EM wave propagating in free space.

This procedure is accurately described by the Stratton-Chu equation [14–16], or electric (magnetic) field integral equation (EFIE/MFIE) for perfect conductor.

The mechanism of 3-D SAR with fixed transmitter is discussed in this paper. In Section 2, the traditional 3-D SAR systems and the scattering center model are reviewed, and the phase reversal phenomenon is discussed based on experimental results. In Section 3,

the signal model of 3-D SAR with fixed transmitter is discussed via Stratton-Chu equation. In Section 4, the physical meanings of the 3-D SAR image for perfect conductor and general dielectric medium are discussed. In Section 5, experimental results of 3-D SAR with fixed transmitter are presented to demonstrate its feasibility to focus corner and cavity-shaped objects, and its possible applications in remote sensing and RCS measurement are discussed. The main conclusions are summarized in Section 6 finally.

2. PROBLEM OF SCATTERING CENTER MODEL

2.1. Review on Present 3-D SAR

According to the application environment, the implementations of 3-D SAR include mainly two classes: rail-based 3-D SAR systems and airborne 3-D SAR systems. The rail-based 3-D SAR systems control the T/R antenna(s) moving via mechanical devices, including stepping motor, rail and screw rod, etc.. The typical operating mode is to move the T/R antenna(s) in 2-D plane and synthesize a full-element aperture, which is named as planar SAR. In recent years, some planar SAR systems have been developed by Pacific Northwest National Laboratory (PNNL) and University of Electronic Science and Technology of China (UESTC), imaging results in dark chamber and out-field are presented respectively.

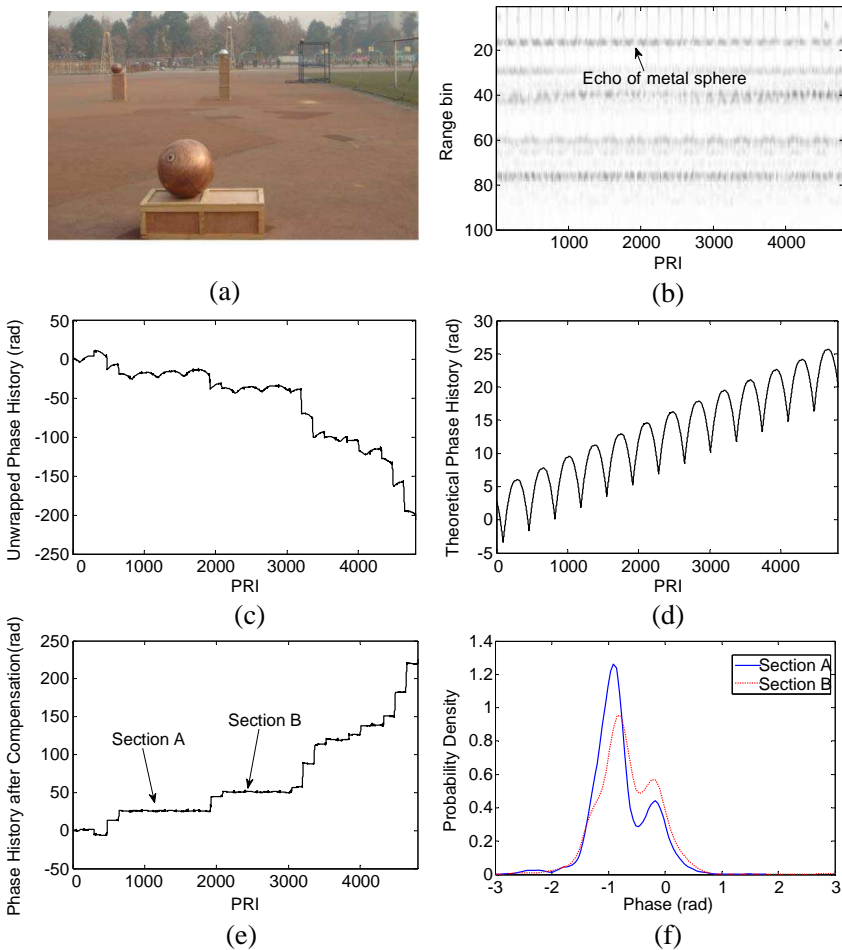
In some cases, the T/R antennas move in a circular orbit and synthesize a ring-shaped aperture, which is named as circular SAR. In 1999, Tsz-King Chan et al. designed the first circular SAR system. In their experiments, the T/R antennas were mounted on two separate wooden rings that were individually driven by stepping motors. Imaging results of a model helicopter have been obtained and published [1].

To overcome the high sidelobes of the ring-shaped aperture and obtain Omni-directional images, a linear T/R antenna array can be controlled to move around the target, and synthesize a cylindrical aperture, which is named as cylindrical SAR. This mode was adopted by a commercial system, ProVision Whole Body Imager, developed by L3-SafeView under the license of PNNL for security inspection and automated body measurement applications. ProVision system is currently deployed around the world at airports, courthouses, military checkpoints, and other governmental and commercial buildings [5].

The airborne 3-D SAR system mounts the T/R antenna(s) on an aircraft and synthesizes a 2-D aperture via the motion of the platform. To synthesize a full-element 2-D array, a linear array should be mounted along the wings. However, the linear array must be rather

long and the number of elements is extremely large, which is difficult and expensive to be implemented to achieve high cross-track resolution. To reduce the system complexity and cost, M. Weiß and J. H. G. Ender introduced the concept “MIMO radar” into the linear array SAR, and designed the ARTINO system [3]. Combining the MIMO technique and sparse array technique, one can synthesize a sparse linear array SAR by activating one or several T/R elements at one PRI, which can reduce the number of data acquisition channels greatly further.

Another existing airborne 3-D SAR system is circular SAR that synthesizes a ring-shaped aperture via controlling the trajectory of aircraft. Some experiments of circular SAR were carried at the Air Force Research Laboratory, and imaging results have been presented [4].



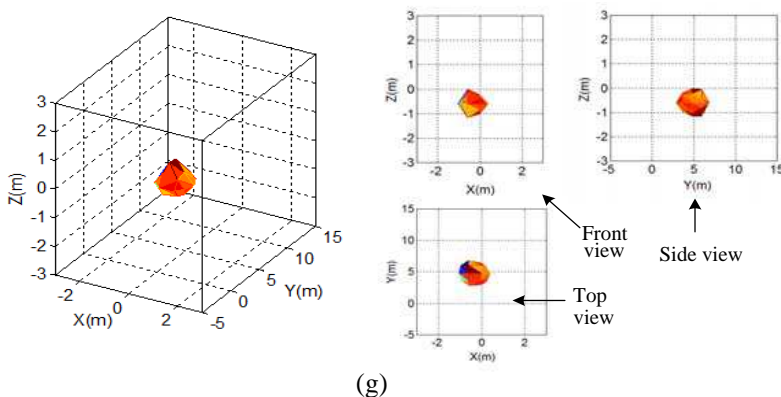


Figure 1. (a) Photo of metal sphere(the forefront), (b) acquired data after range compression, (c) phase history of the metal sphere after phase unwrapping, (d) theoretical phase history of scattering center model, (e) phase history after compensating the theoretical phase, (f) phase probability densities of Sections A and B, (g) imaging result of the sphere.

For all of the above 3-D SAR systems, the T/R antennas move synchronously, just like the traditional 2-D SAR system. Under this circumstance, targets can be modeled using scattering center model that considers the targets as the collection of scattering centers [16] whose scattering coefficients keep constant with respect to the observation angles. This model works well when the aperture angle is relatively small. During the experimental data processing, however, we find that since the actual aperture angle is rather larger, the scattering center model might be invalid for some objects.

2.2. Variation of Scattering Coefficients with Observation Angle

The experimental 3-D SAR imaging system works on X-band with signal bandwidth about 120 MHz and pulse repetition frequency (PRF) 20 Hz. The T/R antennas move synchronously in 2-D plane to produce a 2-D virtual aperture [12].

Figure 1(a) is the photo of the observation scene, a metal sphere is laid at forefront. Figure 1(b) is the acquired (complex) data after range compression, the echoes of the metal sphere locate in the 16th range bin. By selecting the echoes, extracting their phases, and unwrapping the phase ambiguity, the phase history of the metal sphere is obtained, which is shown in Figure 1(c).

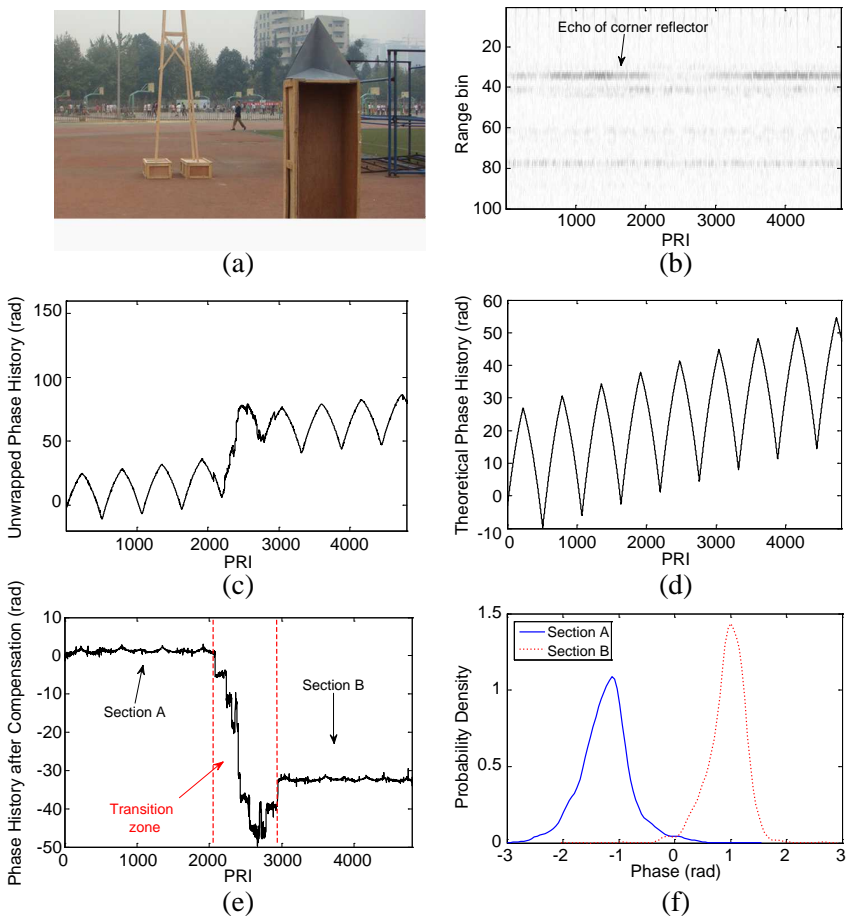
Compensating the phase history using theoretical value (shown

in Figure 1(d)), we obtain the compensated phase history, which is a sectionalized and line-like curve (Figure 1(e)).

Superficially, the experiment data dose not matched the scattering center model properly, which asserts that the compensated phase should be a constant. When fetching the phases of different sections and computing their phase probability densities, however, we find that the densities of them are rather similar, which are plotted in Figure 1(f).

It indicates that though the compensated phase history seems to be irregular, there is a fixed 2π ($2k\pi$ exactly) phase shift, which might occur during the course of phase unwrapping because of phase noise (since the RCS of metal sphere is relatively small, the wooden box and ground might deteriorate its phase history).

Since a 2π phase shift does not affect the imaging processing, we can states that for metal spheres, even with a relatively larger aperture



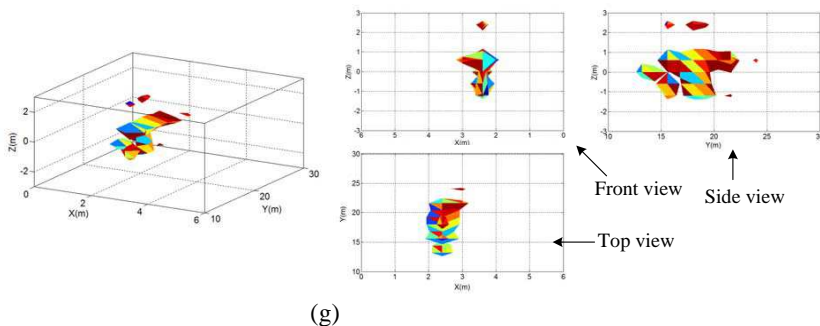


Figure 2. (a) Photo of corner reflector, (b) acquired data after range compression, (c) phase history of the corner reflector after phase unwrapping, (d) theoretical phase history of scattering center model, (e) phase history after compensating the theoretical phase, (f) phase probability densities of Sections A and B, (g) imaging result of the corner reflector (30% threshold).

angle, the scattering center model is still available. Figure 1(g) is the 3-D imaging result of the metal sphere via matched filtering in top-view, side-view, front-view and 3-D view respectively. The isosurface threshold is about 30% of the maximum value. Obviously, the energy concentrates in a local region with size about $1\text{ m} \times 1\text{ m} \times 1\text{ m}$, which matches the system resolutions properly and indicates that the image is well-focused.

When we try to focus a corner reflector (shown in Figure 2(a)) using the same system, however, we find that the energy of the corner reflector cannot be accumulated properly, and is far lower than the expected value by considering it as a scatterer.

Figure 2(c) plots the phase history after phase unwrapping of the corner reflector. Compared with Figure 1(c), we find that the phase history is clearer (shown in Figure 2(d)). The reason is that the RCS of the corner reflector is far larger than those of surroundings, and its phase history has less effect of phase noise.

Figure 2(e) plots the compensated phase history. Just like the metal sphere, the compensated phase history of the corner reflector is sectionalized and line-like curve. When observing the curve carefully, we find that the transition between the two sections (marked as Sections A and B in Figure 2(e)) is wider than those of the metal sphere and fluctuant acutely, which is suspicious to be considered as the fault of phase unwrapping. By analyzing the phase probability densities of different sections further, we find that the difference of the expected phase centers of different sections is about π , i.e., the compensated phases reverse during an observation session, and the scattering center

model is not available any more.

The phase reversal phenomenon can be explained using the electromagnetic theory. According to the reflection and refraction theory, when the index of refraction of reflection medium is smaller than that of refraction medium, such as metal medium, there is a phase reversal for the reflected wave [17]. For 3-D SAR with moving transmitter, the EM wave might bounce several times before arriving the receiver, every bounce will reverse the phase, and lead to the phase reversal phenomenon finally.

Figure 2(g) is the 3-D imaging result of the corner reflector via matched filtering in top-view, side-view, front-view and 3-D view respectively. The isosurface threshold is about 30% of the maximum value. Obviously, the energy spreads in a vast region with size about $1\text{ m} \times 10\text{ m} \times 4\text{ m}$, which indicates the image defocuses severely. Phase reversal might occur when one try to focus corner reflectors or cavity-shaped objects, such as the aircraft inlet, vehicle, etc..

3. SIGNAL MODEL OF 3-D SAR WITH FIXED TRANSMITTER

To avoid the phase reversal phenomenon, an easy-to-understand method is to fix the transmitter during the observation session. Since the geometry between the transmitter and targets is fixed, the induced electric/magnetic currents on the targets keep unchanged, and maintain the coherence of the scattering EM.

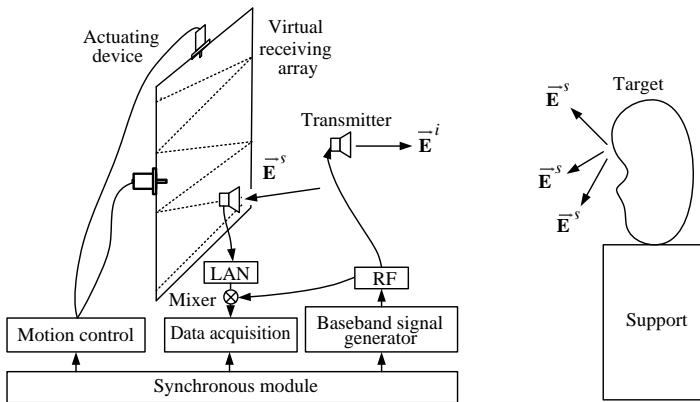


Figure 3. schematic diagram of 3-D SAR with fixed transmitter.

3.1. System Overview

The schematic diagram of 3-D SAR with fixed transmitter is illustrated in Figure 3, which consists mainly of a transmitter, receiver, motion platform and synchronous module. A transmitter is fixed between the receiver and the targets, and radiates periodically the EM wave to the targets. The transmitted signal might be chirp signal or stepped-frequency signal, according to the requirement of range resolution and observation environment. The PRF is selected according to the speed of the motion platform to ensure the displacement of the receiver between the adjacent pulses less than wavelength (for isotropic antenna) to avoid the grating lobes.

The receiver is mounted on the 2-D motion platform, moves in 2-D plane, and acquires the echo. Deramping technique can be used for chirp signal or stepped-frequency signal to reduce the sampling frequency [5]. Matched filtering technique, such as back projection algorithm (BP), can be employed for data processing.

The motion platform controls the receiver's motion and records its trajectory for data processing. The trajectory should carefully be designed to avoid the grating lobes [12].

According to the scattering theory, the mechanism of 3-D SAR with fixed transmitter can be explained via two stages:

1. The incident electromagnetic wave inspires the induced electric/magnetic currents on the targets,
2. The induced electric/magnetic currents produce the scattering electromagnetic wave propagating in free space.

This explanation is very similar to the camera system. The transmitter is analogue to the light source that lights up the targets. Of course, it is allowable to deploy more than one transmitter radiating EM wave synchronously to obtain the desired "lighting effects". The motion platform, receiver and data processor are analogue to the lens and films that focus the rays and record the images. Unlike the camera system, since the EM wave(s) is (are) produced actively, the echoes at different pulses are coherent, and it is feasible to construct a virtual 2-D antenna array using synthetic aperture technique.

3.2. Signal Model in Single-frequency Case

In the viewpoint of scattering center model, 3-D SAR with fixed transmitter works at bistatic mode, and the non-backscattering problem should be considered during modeling. Since the bistatic angle varies continuously during data acquisition, it is a rather complex job to discuss its principle using scattering center model. Thus, the scattering theory is used to build its signal model.

Essentially, the scattering mechanism is dominated by the Maxwell equations, which describe the interaction between the incident EM wave and the scattering EM wave. In free space, the Maxwell equations can be solved as the Stratton-Chu integral equation, which is convenient to analyzing the mechanism of 3-D SAR with fixed transmitter.

Assume that the transmitter is fixed at the original point during the observation session, and the receiver moves in 2-D plane, and records the scattering electric field (exactly, the voltage) of different positions, which is determined by the Stratton-Chu equation [14]:

$$\begin{aligned} \vec{\mathbf{E}}^s = & \int_{V'} \left[j\omega\mu\vec{\mathbf{J}}\psi - \vec{\mathbf{M}} \times \nabla\psi + \frac{\rho}{\varepsilon}\nabla\psi \right] d\mathbf{p}' \\ & + \oint_{S'} \left[j\omega\mu(\hat{\mathbf{n}} \times \vec{\mathbf{H}})\psi + (\hat{\mathbf{n}} \times \vec{\mathbf{E}}) \times \nabla\psi + (\hat{\mathbf{n}} \cdot \vec{\mathbf{E}})\nabla\psi \right] dS' \end{aligned} \quad (1a)$$

where, ω denotes the temporal frequency, μ the permeability, ε the permittivity, $\vec{\mathbf{J}}$ the volume electric current density, $\vec{\mathbf{M}}$ the volume magnetic current density, ρ the free charge density, S' the surface of the target, $\vec{\mathbf{H}}$ and $\vec{\mathbf{E}}$ the magnetic and electric fields respectively, $\hat{\mathbf{n}}$ the normal direction of S' , ∇ the gradient operator, and ψ the green function,

$$\psi \triangleq \frac{e^{jK|\mathbf{p}-\mathbf{p}'|}}{4\pi|\mathbf{p}-\mathbf{p}'|}, \quad (1b)$$

$$\nabla\psi = \frac{(1+jK|\mathbf{p}-\mathbf{p}'|)\hat{\mathbf{p}}}{|\mathbf{p}-\mathbf{p}'|}\psi \quad (1c)$$

$$\mathbf{p} \triangleq (\mathbf{p}-\mathbf{p}')/|\mathbf{p}-\mathbf{p}'| \quad (1d)$$

where, \mathbf{p} denotes the coordinates of scattering field, \mathbf{p}' denotes the coordinates of target, K denotes the spatial frequency, or wave number, $K = \frac{2\pi}{\lambda} = \frac{\omega}{c}$.

The triple integral in Equation (1) represents the scattering field caused by the volume electric/magnetic currents. The surface integral represents the scattering field caused by the surface electric/magnetic currents of conductor.

By introducing the 3-D Dirac function, the surface integral can be absorbed into the triple integral, and we have:

$$\vec{\mathbf{E}}^s = \int_{V'} \left[j\omega\mu\vec{\mathbf{J}}'\psi - \vec{\mathbf{M}}' \times \nabla\psi + \frac{\rho'}{\varepsilon}\nabla\psi \right] d\mathbf{p}' \quad (2)$$

where, $\vec{\mathbf{J}}'$, $\vec{\mathbf{M}}'$ and ρ' contain their counterparts in the surface integral respectively. $\vec{\mathbf{J}}'$, $\vec{\mathbf{M}}'$ and ρ' are simplified as $\vec{\mathbf{J}}$, $\vec{\mathbf{M}}$ and ρ in this paper.

In practice, $K |\mathbf{p} - \mathbf{p}'| \gg 1$, $\nabla\psi \approx jK\hat{\mathbf{p}}\psi$, and Equation (2) can be rewritten as:

$$\vec{\mathbf{E}}^s \approx \int_{V'} \left[j\omega\mu\vec{\mathbf{J}}\psi - jK \left(\vec{\mathbf{M}} \times \hat{\mathbf{p}} \right) \psi + jK \frac{\rho}{\epsilon} \hat{\mathbf{p}}\psi \right] d\mathbf{p}' \quad (3)$$

Equation (3) indicates that the scattering electric field is determined by the electric current density $\vec{\mathbf{J}}$, magnetic current density $\vec{\mathbf{M}}$ and free charge density ρ . In practice, the free charge can be ignored because

1. In many cases, the targets are electrically neutral, and there is no free charge,
2. Even there are some free charges on the observed targets, because its scattering electric field is perpendicular to the polarization direction of the receiving antenna, and can hardly be acquired,
3. Because the scattering field of free charges is non-coherent to the transmitted signal, its energy cannot be enhanced during the imaging processing.

Thus, Equation (3) can be simplified as:

$$\vec{\mathbf{E}}^s \approx \int_{V'} \left[j\omega\mu\vec{\mathbf{J}}\psi - jK \left(\vec{\mathbf{M}} \times \hat{\mathbf{p}} \right) \psi \right] d\mathbf{p}' \quad (4)$$

Denoting the polarization direction of the receiving antenna (idealized dipole) as $\hat{\mathbf{a}}$, the received voltage at position \mathbf{p} is:

$$v(\mathbf{p}, t) = \hat{\mathbf{a}} \cdot \vec{\mathbf{E}}^s = \int_{V'} j\hat{\mathbf{a}} \cdot \left[\omega\mu\vec{\mathbf{J}} - K \left(\vec{\mathbf{M}} \times \hat{\mathbf{p}} \right) \right] \psi d\mathbf{p}' \quad (5)$$

where, t denotes the time domain, which is associated to the time-varying term $e^{j\omega t}$ that has been ignored during the above derivations.

Equation (5) indicates that the voltage function of the receiver can be expressed as the integral of the electric and magnetic current densities. The nature of 3-D SAR with fixed transmitter is to recover the electric/magnetic current densities using the measured voltage data.

3.3. Signal Model in Wideband Case

For 3-D SAR, wideband signals are necessary to obtain high range resolution. Given the transmitted wideband voltage signal $f(t)$, the

receiver's voltage can be expressed as the integral with respect to the temporal frequency, i.e.,

$$v(\mathbf{p}, t) = \int_{-\infty}^{\infty} F(\omega) \left[\int_{V'} j\hat{\mathbf{a}} \cdot [\omega\mu\vec{\mathbf{J}} - K(\vec{\mathbf{M}} \times \hat{\mathbf{p}})] \psi d\mathbf{p}' \right] e^{j\omega t} d\omega \quad (6)$$

where, $F(\omega)$ denotes the Fourier transformation of $f(t)$.

Since $K = \omega c^{-1}$, under the approximation that the $\vec{\mathbf{J}}$ and $\vec{\mathbf{M}}$ are independent to the carrier frequency ω , we have:

$$\begin{aligned} v(\mathbf{p}, t) &= \int_{V'} \frac{\hat{\mathbf{a}} \cdot [\mu\vec{\mathbf{J}} - c^{-1}(\vec{\mathbf{M}} \times \hat{\mathbf{p}})]}{4\pi |\mathbf{p}' - \mathbf{p}|} \left[\int_{-\infty}^{\infty} j\omega F(\omega) e^{j\omega(t-\tau)} d\omega \right] d\mathbf{p}' \\ &= \int_{V'} \frac{\hat{\mathbf{a}} \cdot [\mu\vec{\mathbf{J}} - c^{-1}(\vec{\mathbf{M}} \times \hat{\mathbf{p}})]}{4\pi |\mathbf{p}' - \mathbf{p}|} f'(t - \tau) d\mathbf{p}' \end{aligned} \quad (7)$$

where, $\tau = \tau_T + \tau_R$, $\tau_T = |\mathbf{p}' - \mathbf{p}_T|/c$, $\tau_R = |\mathbf{p}' - \mathbf{p}|/c$, \mathbf{p}_T denotes the position of transmitter, $f'(t)$ denotes the derivative of $f(t)$.

For the chirp signal (LFM), i.e., $f(t) = e^{j(\omega_0 t + \pi\beta t^2)}$, the receiver's voltage can be expressed as:

$$v(\mathbf{p}, t) = \int_{V'} \frac{j\hat{\mathbf{a}} \cdot [\mu\vec{\mathbf{J}} - c^{-1}(\vec{\mathbf{M}} \times \hat{\mathbf{p}})]}{4\pi |\mathbf{p}' - \mathbf{p}|} \alpha(t) e^{j[\omega_0(t-\tau) + \pi\beta(t-\tau)^2]} d\mathbf{p}' \quad (8)$$

where, $\tau |\mathbf{p}' - \mathbf{p}|/c$, $\alpha(t) = \omega_0 + 2\pi\beta(t - \tau)$. Since $\alpha(t)$ is a slowly-varying function, it can be ignored during analysis.

After down-modulation and range-compression, we have:

$$\begin{aligned} v(\mathbf{p}, t) &\approx \int_{V'} \hat{\mathbf{a}} \cdot [\mu\vec{\mathbf{J}} - c^{-1}(\vec{\mathbf{M}} \times \hat{\mathbf{p}})] \varphi(\mathbf{p}, t; \mathbf{p}') d\mathbf{p}' \\ \varphi(\mathbf{p}, t; \mathbf{p}') &\triangleq \frac{j\omega_0 e^{j\omega_0 \tau}}{4\pi |\mathbf{p}' - \mathbf{p}|} \chi_R(t - \tau) \end{aligned} \quad (9)$$

where, $\varphi(\mathbf{p}, \omega; \mathbf{p}')$ denotes the kernel function of wideband scattering integral equation, $\chi_R(\cdot)$ denotes the ambiguity function in the range direction. Equation (9) indicates that 3-D SAR imaging can be divided as a 2-D array imaging (corresponding to $e^{j\omega_0 \tau}$) and a high range resolution compression (corresponding to $\chi_R(\cdot)$).

Note that, since τ_T keeps constant with respect to \mathbf{p} , the transmitter has no contribution to the resolution in the virtual array directions, and their resolution formulas are equal to the radiometer

or passive optical system, i.e., $\rho_A = \lambda R/L$, rather than the traditional SAR $\rho_A = \lambda R/(2L)$. On the other hand, since the transmitter has contribution to the resolution in the range direction, its resolution formula is equal to the traditional SAR, i.e., $\rho_R = c/(2B)$, B denotes the signal bandwidth.

4. EXPLANATION OF 3-D SAR IMAGE WITH FIXED TRANSMITTER

The aim of 3-D SAR imaging is to reconstruct the targets' scattering characteristics from the acquired data. According to the analysis in the last section, however, there are two irreducible unknowns $\vec{\mathbf{J}}$ and $\vec{\mathbf{M}}$ in Equation (5), and it is impossible to solve both of them with one integral equation. Thus, the matched filtering method, such as back projection (BP) algorithm [18, 19], are used to obtain an approximate solution.

4.1. Perfect Conductor

For perfect conductor, the magnetic current density $\vec{\mathbf{M}}$ can be ignored further, and the Stratton-Chu equation is reduced as the electric field integral equation (EFIE) [11]:

$$\vec{\mathbf{E}}^s = j\omega\mu \int_{V'} \left[\vec{\mathbf{J}}\psi + \frac{1}{K^2}(\nabla \cdot \vec{\mathbf{J}})\nabla\psi \right] d\mathbf{p}' \quad (10)$$

Analogously to the analysis in the last section, Equation (10) can be simplified as:

$$v(\mathbf{p}, \omega) \approx \int_{V'} J_a \varphi(\mathbf{p}, \omega; \mathbf{p}') d\mathbf{p}' \quad (11)$$

$$J_a = \mu \hat{\mathbf{a}} \cdot \vec{\mathbf{J}}$$

The matched filtering method approximates $J_a(\mathbf{p}')$ by the following formula:

$$\tilde{J}_a(\mathbf{p}'') \triangleq \frac{1}{N} \int \sum_{\mathbf{p}} v(\mathbf{p}, \omega) \varphi^{-1}(\mathbf{p}'', \mathbf{p}, \omega) d\omega \quad (12a)$$

$$\varphi^{-1}(\mathbf{p}'', \mathbf{p}, \omega) \triangleq \frac{4\pi |\mathbf{p} - \mathbf{p}''|}{j\omega_0} e^{-j\omega_0\tau} \delta(\omega - \beta\tau) \quad (12b)$$

where, \mathbf{p}'' denotes the coordinates of image space, $\delta(\omega)$ denotes the Dirac function.

Substituting Equation (11) into Equation (12a), we have:

$$\begin{aligned}\tilde{J}_a(\mathbf{p}'') &= \int \left[\frac{1}{N} \sum_{\mathbf{p}} \int_{V'} J_a \varphi(\mathbf{p}, \omega; \mathbf{p}') d\mathbf{p}' \varphi^{-1}(\mathbf{p}, \omega; \mathbf{p}'') \right] d\omega \\ &= \int_{V'} J_a \left[\int \frac{1}{N} \sum_{\mathbf{p}} \varphi(\mathbf{p}, \omega; \mathbf{p}') \varphi^{-1}(\mathbf{p}, \omega; \mathbf{p}'') d\omega \right] d\mathbf{p}' \\ &= \int_{V'} J_a \chi_{\mathbf{J}}(\mathbf{p}'', \mathbf{p}') d\mathbf{p}'\end{aligned}\quad (13a)$$

$$\chi_{\mathbf{J}}(\mathbf{p}'', \mathbf{p}') \triangleq \int \left[\frac{1}{N} \sum_{\mathbf{p}} e^{-j\omega_0(\tau''-\tau)} \delta(\omega - \beta(\tau'' - \tau)) \right] d\omega \quad (13b)$$

where, $\tau'' |\mathbf{p} - \mathbf{p}''|/c$, $\chi_{\mathbf{J}}(\mathbf{p}'', \mathbf{p}')$ denotes the ambiguity function (or point spread function) corresponding to the electric current density.

For 3-D SAR imaging system, $\tau'' = \tau$ is equivalent to $\mathbf{p}'' = \mathbf{p}'$ [12]. When $\mathbf{p}'' = \mathbf{p}'$, we have:

$$\chi_{\mathbf{J}}(\mathbf{p}', \mathbf{p}') = \int \left[\frac{1}{N} \sum_{\mathbf{p}} \delta(\omega) \right] d\omega = 1, \quad (14)$$

which is the maximum of $\chi_{\mathbf{J}}(\mathbf{p}'', \mathbf{p}')$.

When $\mathbf{p}'' \neq \mathbf{p}'$, $\chi_{\mathbf{J}}(\mathbf{p}'', \mathbf{p}')$ is the sum of a complex exponential function, which can be considered as zero under the condition that the imaging system is well-designed.

Approximating $\chi_{\mathbf{J}}(\mathbf{p}'', \mathbf{p}') = 0$ $\mathbf{p}'' \neq \mathbf{p}'$, $\chi_{\mathbf{J}}(\mathbf{p}'', \mathbf{p}')$ is a 3-D Dirac function, and we have:

$$\tilde{J}_a(\mathbf{p}') \approx J_a(\mathbf{p}') \quad (15)$$

Equation (15) indicates that the imaging results of 3-D SAR with fixed transmitter are the estimations of the electric current density for perfect conductor. Since $\chi_{\mathbf{J}}(\mathbf{p}'', \mathbf{p}')$ is not zero exactly when $\mathbf{p}'' \neq \mathbf{p}'$, the values of different scatterers will interfere to each other, which lead to additional measurement errors.

Furthermore, according to Equation (11), for perfect conductor, there is only unknown variable J_a . Thus, the imaging problem can be considered as solving an integral equation, and some advanced signal processing method, such as sparse recovery technique [20–22], can be employed to eliminated the sidelobes of matched filtering method.

4.2. General Case

For general medium, both $\vec{\mathbf{J}}$ and $\vec{\mathbf{M}}$ affect the scattering EM filed. Substituting Equation (9) into Equation (12a), we have the imaging result of matched filtering method:

$$\begin{aligned} & \tilde{X}_a(\mathbf{p}'') \\ & \triangleq \int \left[\frac{1}{N} \sum_{\mathbf{p}} \left(\int_{V'} \mu \hat{\mathbf{a}} \cdot \vec{\mathbf{J}} \varphi(\mathbf{p}, \omega; \mathbf{p}') dV' \right) \varphi^{-1}(\mathbf{p}, \omega; \mathbf{p}'') \right] d\omega \\ & - \int \left[\frac{1}{N} \sum_{\mathbf{p}} \left(\int_{V'} c^{-1} \hat{\mathbf{a}} \cdot (\vec{\mathbf{M}} \times \hat{\mathbf{p}}) \varphi(\mathbf{p}, \omega; \mathbf{p}') dV' \right) \varphi^{-1}(\mathbf{p}, \omega; \mathbf{p}'') \right] d\omega \end{aligned} \quad (16)$$

The first term represents the volume electric current density, which is equal to $\tilde{J}_a(\mathbf{p}')$. The second term represents the volume magnetic current density.

Just as the previous discussion, when $\mathbf{p}'' \neq \mathbf{p}'$, we have:

$$\int \frac{1}{N} \sum_{\mathbf{p}} \left(\int_{V'} c^{-1} \hat{\mathbf{a}} \cdot (\vec{\mathbf{M}} \times \hat{\mathbf{p}}) \varphi(\mathbf{p}, \omega; \mathbf{p}') dV' \right) \varphi^{-1}(\mathbf{p}, \omega; \mathbf{p}'') d\omega \approx 0 \quad (17)$$

when $\mathbf{p}'' = \mathbf{p}'$, we have:

$$\begin{aligned} & \int \left[\frac{1}{N} \sum_{\mathbf{p}} \left(\int_{V'} c^{-1} \hat{\mathbf{a}} \cdot (\vec{\mathbf{M}} \times \hat{\mathbf{p}}) \varphi(\mathbf{p}, \omega; \mathbf{p}') dV' \right) \varphi^{-1}(\mathbf{p}, \omega; \mathbf{p}'') \right] d\omega \\ & = \int \left[\frac{1}{N} \sum_{\mathbf{p}} \left(\int_{V'} c^{-1} \hat{\mathbf{a}} \cdot (\vec{\mathbf{M}} \times \hat{\mathbf{p}}) \delta(\omega) dV' \right) \right] d\omega \\ & = \int_{V'} c^{-1} \hat{\mathbf{a}} \cdot \left(\vec{\mathbf{M}} \times \frac{1}{N} \sum_{\mathbf{p}} \hat{\mathbf{p}} \right) dV' \end{aligned} \quad (18)$$

thus,

$$\tilde{X}(\mathbf{p}') \approx \int_{V'} J_a \chi_J(\mathbf{p}'', \mathbf{p}') d\mathbf{p}' - \int_{V'} M_a \chi_M(\mathbf{p}'', \mathbf{p}') d\mathbf{p}' \quad (19a)$$

$$M_a \triangleq c^{-1} \hat{\mathbf{a}} \cdot \left(\vec{\mathbf{M}} \times \frac{1}{N} \sum_{\mathbf{p}} \hat{\mathbf{p}} \right) \quad (19b)$$

where, $\chi_M(\mathbf{p}'', \mathbf{p}')$ denotes the ambiguity function corresponding to the magnetic current density.

Strictly speaking, the sidelobes of $\chi_J(\mathbf{p}'', \mathbf{p}')$ and $\chi_M(\mathbf{p}'', \mathbf{p}')$ are different, and Equation (19a) **cannot** be expressed as:

$$\tilde{X}(\mathbf{p}') \approx \int_{V'} (J_a - M_a) \chi(\mathbf{p}'', \mathbf{p}') d\mathbf{p}' \quad (20)$$

Approximating $\chi_M(\mathbf{p}'', \mathbf{p}') = 0 \mathbf{p}'' \neq \mathbf{p}'$, however, we have:

$$\tilde{X}(\mathbf{p}') \approx J_a(\mathbf{p}') - M_a(\mathbf{p}') \quad (21)$$

$\frac{1}{N} \sum_{\mathbf{p}} \hat{\mathbf{p}}$ indicates the composition vector of the directional vectors from the array's elements to the scatterer \mathbf{p}' , which is shown in Figure 4(a).

Since the perpendicular components of $\hat{\mathbf{p}}$ cancel to each other, the composition vector is approximately parallel to $\hat{\mathbf{p}}'$, the unit vector from original point to scatterer \mathbf{p}' , but is slightly shorter. Thus, we have:

$$\tilde{X}_a(\mathbf{p}') \approx J_a(\mathbf{p}') - c^{-1} \hat{\mathbf{a}} \cdot (\vec{\mathbf{M}} \times \eta \hat{\mathbf{p}}') \quad (22)$$

where, η represents the system deviation of 3-D imaging system caused by the magnetic current density, $\eta < 1$.

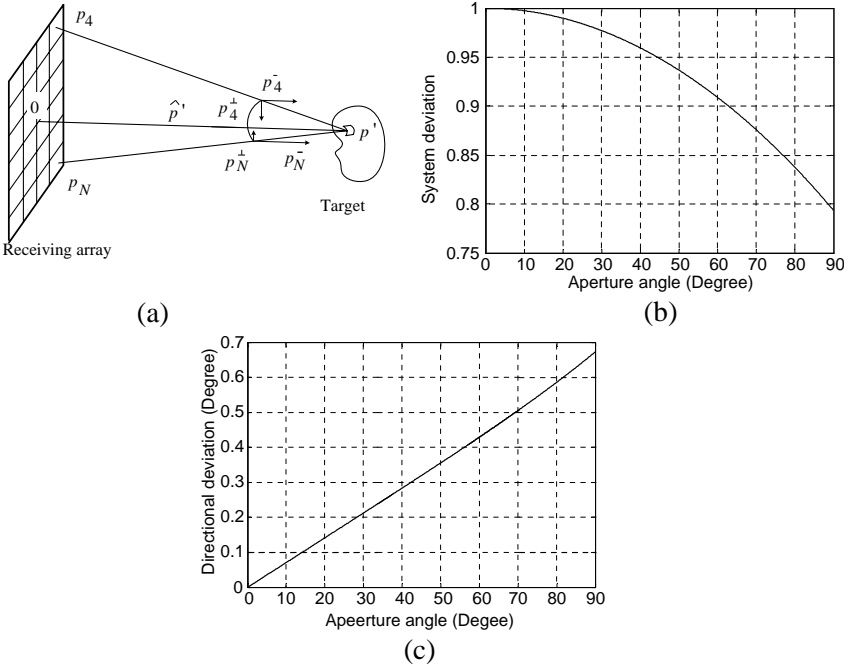


Figure 4. (a) Illustration of the composition vector, (b) relationship between system deviation and aperture angle, (c) directional deviation between the composition vector and $\hat{\mathbf{p}}'$.

Assume that the virtual array is a square array with N^2 elements and interval d , η is the sum of the projection of $\hat{\mathbf{p}}$ onto $\hat{\mathbf{p}}'$ for all elements, i.e.,

$$\eta = \frac{1}{N^2} \sum_{k=-N/2}^{N/2-1} \sum_{l=-N/2}^{N/2-1} \left\langle \frac{\mathbf{p} - \mathbf{p}'}{\|\mathbf{p} - \mathbf{p}'\|_2}, \hat{\mathbf{p}}' \right\rangle \quad (23)$$

$$\mathbf{p} = (kd \quad ld \quad 0)$$

By some simple derivations, we find that, when there is only one receiving element at the original point, i.e., $N^2 = 1$, $\eta = 1$.

Figure 4(b) plots the relationship between the system deviation and the aperture angle. From it, we can say that η decreases with the increase of the aperture angles. When the aperture angle is smaller than 20 degree (corresponding to 3λ spatial resolution), $\eta > 0.98$, which can be ignored in practice.

Figure 4(c) shows the directional deviation between the composition vector and $\hat{\mathbf{p}}'$. We find that when the aperture angle is smaller than 20 degree, the directional deviation can also be ignored.

Under this approximation, Equation (22) can finally be approximated as:

$$\tilde{X}_a(\mathbf{p}') \approx J_a(\mathbf{p}') - c^{-1} \hat{\mathbf{a}} \cdot (\vec{\mathbf{M}} \times \hat{\mathbf{p}}') \quad (24)$$

Equation (24) indicates that the (complex) value of the matched filtering method is proportional to the superposition of the volume electric current density $\vec{\mathbf{J}}$ and the outer product of the volume magnetic current density $\vec{\mathbf{M}}$ and the unit vector from the virtual array center to the scatterer $\hat{\mathbf{p}}'$.

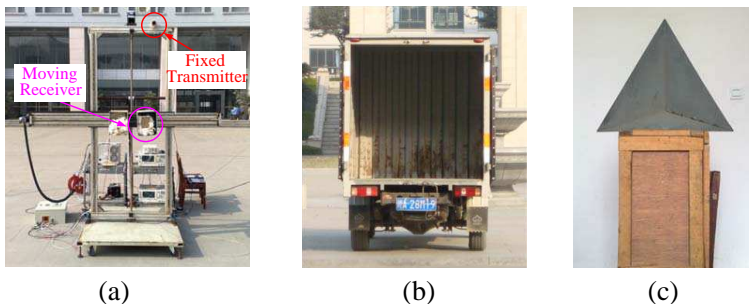


Figure 5. (a) photo of 3-D SAR with fixed transmitter, the transmitter is mounted on the top of the 2-D platform, (b) photo of a goods van, (c) photo of a corner reflector.

5. EXPERIMENTAL RESULTS AND DISCUSSION

5.1. Experimental Results

To verify the performance of 3-D SAR with fixed transmitter, some preliminary experiments are carried. The experimental system is same with the one introduced in Section 2, except that the transmitter is mounted on the top of the 2-D platform, which is shown in Figure 5(a), and only the receiver moving in 2-D plane. The observed objects are a goods van and a corner reflector, which are shown in Figures 5(b) and (c) respectively.

The first experiment observes the empty goods box only, whose outline is shown in Figure 6(a). Figures 6(b) and (c) are the imaging result (amplitudes are displayed in logarithm mode) of the empty goods box in 3-D view, side-view, top-view and front-view respectively. From it, we find that the imaging result is a hollow cube with size about $2\text{ m} \times 2\text{ m} \times 1.5\text{ m}$ (note that to observe the details, the scale of Figures 6

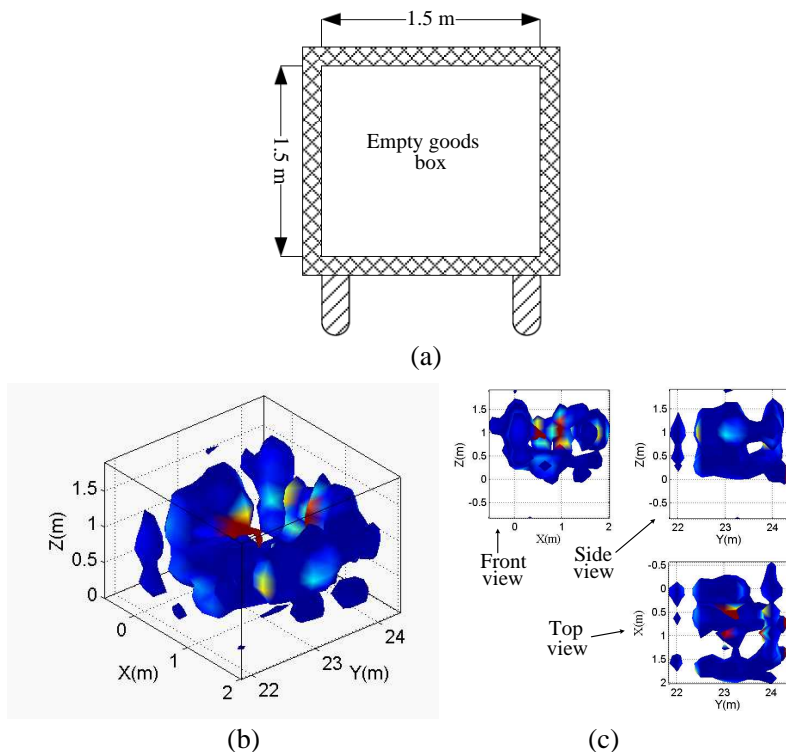


Figure 6. (a) Illustration of the empty goods box, (b) imaging result of empty goods box, which is a hollow cube, (c) side-view, top-view and front-view images respectively.

and 7 is smaller than that of Figures 1 and 2), and reflects the shape of the empty goods box soundly.

In the second experiment, a corner reflector is placed in the goods box, which is illustrated in Figure 7(a). Figures 7(b) and (c) are the imaging result of the goods box and corner reflector in 3-D view, side-view, top-view and front-view respectively. Compared with Figure 6(b), we find that there is an evident scatterer in the middle of the hollow cube. Comparing with Figure 2(g), we find that the corner reflector is focused properly with size about 1 m 1.5 m 1 m, which matches the system resolutions properly.

Note that since the energy of the corner reflector is far larger than the goods box, to display its outline, the isosurface threshold is about 15% of the maximum value (-16 dB), rather than 30% (-10 dB). Thus, the sidelobe of the corner reflector appears at position about (1 m, 22 m, 1 m), and the corner reflector's size is larger than the metal sphere in Figure 1(g) (the sizes of both of them are smaller than the

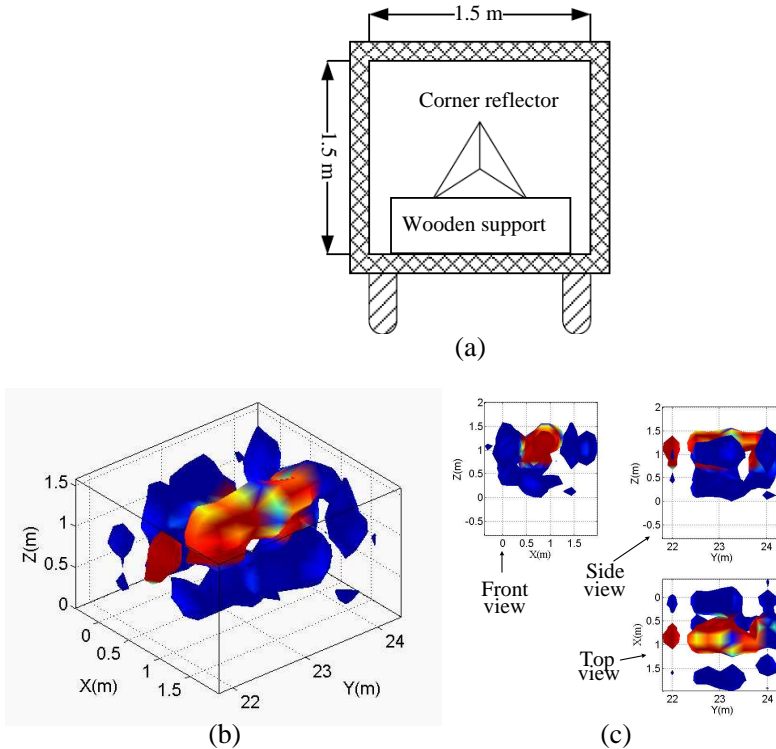


Figure 7. (a) Illustration of the goods box with a corner reflector herein, (b) imaging result of goods box and corner reflector, (c) side-view, top-view and front-view images respectively.

system resolutions.). To avoid the full picture is occupied by the same color (such as blue) and improve the exhibition effect, the middle and surround of the 3-D image are colored with different colormaps.

According to the analysis above, we conclude that by fixing the transmitter, one can focus corner reflectors and cavity-shaped objects, which might fail for 3-D SAR with moving-transmitter because of the phase reversal phenomenon.

5.2. Consideration on Possible Applications

The most remarkable feature of 3-D SAR with fixed transmitter is that it can overpass the scattering center model, build the direct and accurate relationship between the 3-D image and targets' electric/magnetic current densities (reflecting the target's material properties), and connect 3-D SAR imaging technique to scattering theory ultimately. Since its physical meaning is clearer than those of the traditional SAR systems, 3-D SAR with fixed transmitter could be considered as an EM characteristic measurement/analysis device, rather than an imaging tool only.

In the field of remote sensing, combining with scattering theory, the imaging results can be used to analyze the targets' material properties more accurately, especially in high-resolution case, which is important for intensive geoscience researches [23–25]. Secondly, by overcoming the spatial variation of scattering characteristic, high-resolution 3-D images are compatible to the traditional 2-D high/medium resolution SAR images, and are suitable to construct 3-D EM scattering characteristic library of interested objects, which are useful for SAR image classification and recognition applications.

Furthermore, 3-D SAR imaging technique can spatially distinguish the scattering characteristic of the different parts of complex objects. By selecting the ROI manually (pick out the electric/magnetic currents in the ROI using the prior information on the target's shape), or by cancellation technique (for example, subtract the image of the empty goods box from the "goods box + corner reflector" image), we can obtain the scattering characteristic in the ROI, and calculate its RCS easily.

6. CONCLUSION

This paper researches 3-D SAR with fixed transmitter; the main conclusions are presented as follows:

1. Because of the phase reversal phenomenon, 3-D SAR with moving transmitter might fail for corner-shaped objects. Phase

reversal problem can be overcome by fixing the transmitter. The mechanism of 3-D SAR with fixed transmitter can accurately be explained via Stratton-Chu equation.

2. Matched filtering method can reconstruct 3-D images properly. For perfect conductor, 3-D images are proportional to the surface electric current densities. For general medium, 3-D images are the superposition of the volume electric current densities and the outer products of the volume magnetic current densities and the unit vectors from the virtual array centers to the scatterers.

7. FURTHER WORK

Coherence is the fundamental of synthetic aperture technique. This work proposes a feasible method to guarantee the coherence for a relative large aperture angle based on some preliminary experiments and derivations. The validities of the proposed method and signal model will be verified further via accurate EM scattering simulation and more intensive experiments. The possible applications discussed in this paper will also be carried out and verified in the future.

ACKNOWLEDGMENT

This work was supported by the National Natural Science Foundation of China under Grant (No. 61101170).

The authors are with Lab. B504, School of Electronic Engineering, University of Electronic Science and Technology of China, 610054, Chengdu, P. R. China.

REFERENCES

1. Chan, T.-K., Y. Kuga, and A. Ishimaru, "Experimental studies on circular SAR imaging in clutter using angular correlation function technique," *IEEE Transactions on Geoscience and Remote Sensing*, Vol. 37, No. 5, Part 1, 2192–2197, 1999.
2. Bryant, M. L., L. L. Gostin, and M. Soumekh, "3-D E-CSAR imaging of a T-72 tank and synthesis of its SAR reconstructions," *IEEE Trans. on Aerospace and Electronic Systems*, Vol. 39, No. 1, 211–227, 2003.
3. Weiß, M. and J. H. G. Ender, "A 3D imaging radar for small unmanned airplanes — ARTINO," *Proceedings of EURAD 2005 Conference*, 229–232, Oct. 2005.

4. Ertin, E., C. D. Austin, S. Sharma, R. L. Moses, and L. C. Potter, "GOTCHA experience report: Three-dimensional SAR imaging with complete circular apertures," *Proceedings of SPIE — The International Society for Optical Engineering*, v 6568, Algorithms for Synthetic Aperture Radar Imagery XIV, 2007.
5. Sheen, D., D. McMakin, and T. Hall, "Near-field three-dimensional radar imaging techniques and applications," *Applied Optics*, Vol. 49, No. 19, E83–E93, Jul. 2010.
6. Mohammadpoor, M., R. S. A. Raja Abdullah, A. Ismail, and A. F. Abas, "A circular synthetic aperture radar for on-the-ground object detection," *Progress In Electromagnetics Research*, Vol. 122, 269–292, 2012.
7. Qi, Y., W. Tan, Y. Wang, W. Hong, and Y. Wu, "3D bistatic omega-K imaging algorithm for near range microwave imaging systems with bistatic planar scanning geometry," *Progress In Electromagnetics Research*, Vol. 121, 409–431, 2011.
8. Ren, B. L., S. Y. Li, and H. J. Sun, "Modified cylindrical holographic algorithm for three-dimensional millimeter-wave imaging," *Progress In Electromagnetics Research*, Vol. 128, 519–537, 2012.
9. Liu, Q., W. Hong, and W.-X. Tan, "Efficient geosynchronous circular SAR raw data simulation of extended 3-D scenes," *Progress In Electromagnetics Research*, Vol. 127, 335–350, 2012.
10. Austin, C. D., E. Ertin, and R. L. Moses, "Sparse signal methods for 3-D radar imaging," *IEEE Journal of Selected Topics in Signal Processing*, Vol. 5, No. 3, 408–423, Jun. 2011.
11. Zhuge, X. and A. G. Yarovoy, "A sparse aperture MIMO-SAR-based UWB imaging system for concealed weapon detection," *IEEE Transactions on Geoscience and Remote Sensing*, Vol. 49, No. 1, Part 2, 509–518, Jan. 2011.
12. Shi, J., X. Zhang, J. Yang, and C. Wen, "APC trajectory design for "one-active" linear-array three-dimensional imaging SAR," *IEEE Transactions on Geoscience and Remote Sensing*, Vol. 48, No. 3, 1470–1486, Mar. 2010.
13. Soumekh, M., *Synthetic Aperture Radar Signal Processing with MATLAB Algorithms*, 1–261, Wiley-Interscience Inc., 1999.
14. Knott, E. F., J. F. Shaeffer, and M. T. Tuley, *Radar Cross Section, Its Prediction, Measurement and Reduction*, 47–187, Artech House, Inc., Dedham, MA, 1985.
15. Sheppard, C. J. R., A. Choudhury, and J. Gannaway, "Electromagnetic field near the focus of wide-angular lens and

- mirror systems,” *Microwaves, Optics and Acoustics*, Vol. 1, No. 4, 129–132, Jul. 1977.
16. Odendaal, J. W. and J. Joubert, “Radar cross section measurements using near-field radar imaging,” *IEEE Transactions on Instrumentation and Measurement*, Vol. 45, No. 6, 948–954, Dec. 1996.
 17. Jackson, J. D., *Classical Electrodynamics*, 3rd Edition, 302–306, John Wiley & Sons Inc., 1999.
 18. Shi, J., X. Zhang, J. Yang, and Y. Wang, “Surface-tracing-based LASAR 3-D imaging method via multiresolution approximation,” *IEEE Transactions on Geoscience and Remote Sensing*, Vol. 46, No. 11, Part 2, 3719–3730, Nov. 2008.
 19. Liao, K.-F., X.-L. Zhang, and J. Shi, “FAST 3-D microwave imaging method based on subaperture approximation,” *Progress In Electromagnetics Research*, Vol. 126, 333–353, 2012.
 20. Bruckstein, A. M., D. L. Donoho, and M. Elad, “From sparse solutions of systems of equations to sparse modeling of signals and images,” *SIAM Review*, Vol. 51, No. 1, 34–81, 2009.
 21. Shi, J., X. Zhang, J. Yang, and X. Gao, “Signal processing for microwave array imaging: TDC and sparse recovery,” *IEEE Transactions on Geoscience and Remote Sensing*, No. 99, 1–15, 2012.
 22. Wei, S.-J., X.-L. Zhang, and J. Shi, “Linear array SAR imaging via compressed sensing,” *Progress In Electromagnetics Research*, Vol. 117, 299–319, 2011.
 23. Skriver, H., F. Mattia, G. Satalino, A. Balenzano, V. R. N. Pauwels, N. E. C. Verhoest, and M. Davidson, “Crop classification using short-revisit multitemporal SAR data,” *IEEE Journal of Selected Topics in Applied Earth Observations and Remote Sensing*, Vol. 4, No. 2, 423–431, 2011.
 24. Lardeux, C., P.-L. Frison, C. Tison, J.-C. Souyris, B. Stoll, B. Fruneau, and J.-P. Rudant, “Classification of tropical vegetation using multifrequency partial SAR polarimetry,” *IEEE Geoscience and Remote Sensing Letters*, Vol. 8, No. 1, 133–137, 2011.
 25. Prakash, R., D. Singh, and N. P. Pathak, “The effect of soil texture in soil moisture retrieval for specular scattering at C-band,” *Progress In Electromagnetics Research*, Vol. 108, 177–204, 2010.